Int. J. Solids Structures Vol. 22, No. 11, pp. 1243–1257, 1986
Printed in Great Britain.

0020-7683/86 $3.00 + .00
Pergamon Journals Ltd.

PLANE STRAIN NECK PROPAGATION

L. O. FAGER AND J. L. BASSANI
Department of Mechanical Engineering and Applied Mechanics, University of Pennsylvania, Philadelphia, PA 19104, U.S.A.

(*Received* 10 *December* 1984; *in revised form* 24 *September* 1985)

Abstract—Quasi-static neck propagation in polymers (cold drawing) is studied for the case of plane strain tension. For a J_2-deformation theory material (nonlinear elastic), jump conditions across the neck provide a simple steady-state solution. For a J_2-flow theory material a finite element solution characterizes the complete development of a neck in an initially smooth specimen. The numerical results include the overall load–deflection curve, details of deformation states, and the triaxial stress distribution. The solution algorithm is based on a convected coordinate description of the governing equations (Lagrangian in character) with both Newton equilibrium iterations and a stress integration algorithm to improve accuracy.

1. INTRODUCTION

The onset of necking in a macroscopically uniform tensile specimen of a ductile material occurs at load maximum (P_{max}) and is often associated with the growth of a microscopic imperfection. The mechanical state at maximum load is characterized by the condition that the geometric softening due to a local reduction of cross-section is equal to the material hardening. For many materials including most metals and ceramics the material hardening or tangent modulus $E_t = d\sigma/d\varepsilon$ is a monotonically decreasing function of strain and this leads to localized necking with continued elongation up to fracture. A typical true stress (σ)–logarithmic strain (ε) curve for these materials and a load (P)–deflection (Δ) curve for a typical tensile test are depicted in Fig. 1.

Many polymers (e.g. polyethylene and polyvinyl chloride), on the other hand, display σ–ε and P–Δ curves that are shown in Fig. 2[1]. At the onset of necking at P_{max}, $d\sigma/d\varepsilon$ is a decreasing function of strain which accounts for the early stage of neck development. Once the strain in the minimum cross-section of the neck reaches a large enough value the material begins to stiffen with $d\sigma/d\varepsilon$ increasing with increasing strain.† This tends to stabilize the neck and with continued overall elongation the neck propagates. The sequence of events from the onset of necking to neck propagation is depicted in Fig. 3.

Neck propagation, or commonly termed cold drawing, is a standard technique used to orient the molecular chains of the polymer and thereby harden the polymer for products such as fibers (axisymmetric deformation) and magnetic tape and sheet materials (plane strain deformations). Experimental studies of cold drawing are presented by G'Sell *et al.* [1, 3]. Except under conditions of very slow neck propagation, frictional heating of the polymer undergoing large deformations brings thermodynamic considerations into the problem. Nevertheless, the phenomenon of neck propagation is fundamentally a mechanical one and, therefore, the problem considered in this paper is for quasi-static deformations and isothermal conditions.

In a recent study Hutchinson and Neale[4] consider steady-state, axisymmetric neck propagation along circular cylindrical bars. For a nonlinear elastic solid described by J_2-deformation theory they determine the states on both sides of the neck from the jump conditions (across the neck) that result from conservation of mass, momentum and energy. An approximate solution is given for an elastic-plastic solid described by J_2-flow theory that is based upon introducing a parameterized stream function into a variational principle.

† On a molecular level the decreasing tangent modulus, E_t, at relatively small strains is associated with the breaking of weak van der Waals bonds between the long entangled polymer molecules. The subsequent increase in E_t with strain results from the alignment of the molecular chains[2].

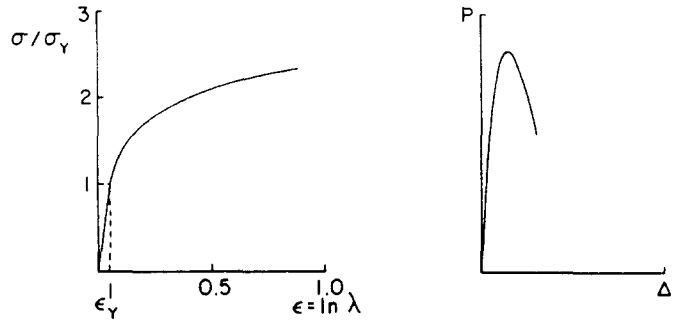

Fig. 1. Typical uniaxial (a) true stress (σ)–logarithmic strain (ε) curve and (b) load (P)–elongation (Δ) curve for metals.

A complete finite element solution for neck formation and propagation in a circular bar of elastic-plastic material is given in a very recent paper by Neale and Tugcu[5].

In this paper neck propagation is analyzed under plane strain deformations. For a nonlinear elastic material described by J_2-deformation theory, jump conditions alone provide a simple solution for the steady-state propagation load and draw ratio. The draw ratio is defined as the ratio between the stretching in the necked-down region to the stretching in the unnecked region. Finite element results based on a J_2-flow theory elastic-plastic material[6] display the development of the neck from an initially smooth configuration. For the material characterization used in the analysis the strains in the necked region are on the order of unity. The finite element algorithm incorporates a Lagrangian formulation of the governing equations[7] to account for the finite changes in geometry.

2. NECK PROPAGATION IN AN INCOMPRESSIBLE, NONLINEAR ELASTIC MATERIAL

The typical shape of the true stress (σ)–logarithmic strain (ε) curves for polymers under monotonic extension in simple tension is depicted in Fig. 2. The tangent modulus $E_t = \mathrm{d}\sigma/\mathrm{d}\varepsilon$ is the slope of this curve and it characterizes the strain hardening of the material. The initial decrease in the tangent modulus followed by a rapid increase at strains on the order of unity is what gives rise to stable neck propagation. The experimental results of G'Sell *et al.*[1, 3] on high density polyethylene indicate that the flow stress $\sigma \propto \exp(M\varepsilon^2)$ at large strains, where M is a positive constant. In this case, $E_t \propto (2M\varepsilon)\exp(M\varepsilon^2)$, which clearly increases with strain. A complete characterization of the uniaxial stress–strain behavior that approximates the shape of Fig. 2 is

$$\sigma = \sigma_Y \begin{cases} \varepsilon/\varepsilon_Y, & 0 \leqslant \varepsilon \leqslant \varepsilon_Y, \\ \alpha(\varepsilon - \varepsilon_P)^N, & \varepsilon_Y \leqslant \varepsilon \leqslant \varepsilon_L, \\ \beta \exp(M\varepsilon^2), & \varepsilon \geqslant \varepsilon_L. \end{cases} \tag{2.1}$$

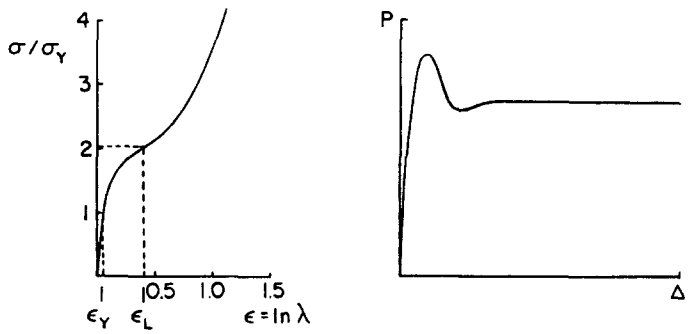

Fig. 2. (a) Uniaxial true stress (σ)–logarithmic strain (ε) curve for a polymer [from eqn (2.2)] and (b) typical uniaxial load (P)–elongation (Δ) behavior for a polymer test specimen.

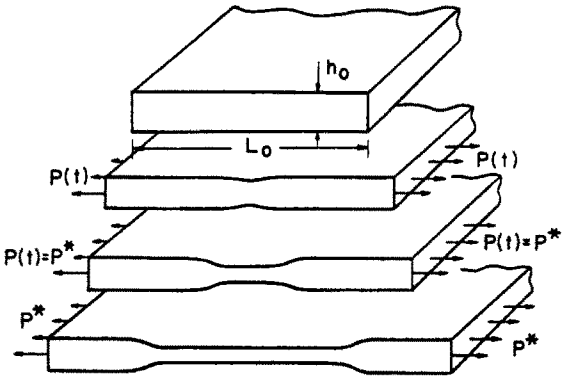

Fig. 3. Sequence of deformation states depicting plane strain neck formation and propagation.

Continuity of σ and $d\sigma/d\varepsilon$ at both the yield strain, ε_Y, and the "locking strain", ε_L, determines four of the eight material constants σ_Y, ε_P, ε_Y, ε_L, α, β, N and M in terms of the other four Equation (2.1) differs slightly in initial plastic response from the ones used in previous analyses[4, 5], where here the term ε_p is introduced to accommodate continuity of σ and $d\sigma/d\varepsilon$ at both ε_Y and ε_L. Throughout this paper, results will be presented for a material with $\varepsilon_Y = 0.05$, $\varepsilon_L = 0.4$ and $N = 0.2$. In this case, eqn (2.1) takes the form

$$\sigma = \sigma_Y \begin{cases} 20\varepsilon, & 0 \leqslant \varepsilon \leqslant 0.05, \\ 2.51(\varepsilon - 0.04)^{0.2}, & 0.05 \leqslant \varepsilon \leqslant 0.4, \\ 1.83 \exp(0.69\varepsilon^2), & \varepsilon \geqslant 0.4. \end{cases} \tag{2.2}$$

The stress–strain curve plotted in Fig. 2 is based on eqn (2.2).

For purely elastic material behavior, an isotropic and incompressible multiaxial generalization of any uniaxial σ–ε curve, including (2.1), is given in terms of J_2-deformation theory[4]:

$$s_{ij} = \tfrac{2}{3} E_s \varepsilon_{ij}, \tag{2.3}$$

where s_{ij} are the Cartesian components of the Cauchy stress (σ) deviator

$$s_{ij} = \sigma_{ij} - (\sigma_{kk}/3)\,\delta_{ij} \tag{2.4}$$

and ε_{ij} are the Cartesian components of the logarithmic strain tensor ε that has principal values $\varepsilon_i = \ln \lambda_i$, where λ_i are the principal stretches. In uniaxial extension of a bar of initial length L_0 and current length L, for example, $\lambda \equiv L/L_0$. The secant modulus, E_s, is determined from the uniaxial σ–ε curve [e.g. eqn (2.1)] at the effective stress level

$$\sigma_e = (\tfrac{3}{2} s_{ij} s_{ij})^{1/2}. \tag{2.5}$$

In terms of the effective strain

$$\varepsilon_e = (\tfrac{2}{3} \varepsilon_{ij} \varepsilon_{ij})^{1/2} \tag{2.6}$$

it is straightforward to show from eqn (2.3) that $E_s = \sigma_e/\varepsilon_e$. Under plane strain tension $\sigma_{11} = \sigma$ and $\varepsilon_{33} = 0$, and it follows from eqns (2.3)–(2.6) that $\sigma_e = (\sqrt{3}/2)\sigma$ and $\varepsilon_e = (2/\sqrt{3})\varepsilon$ are the effective (simple tension) measures of this state.

With $E_s = \sigma_e/\varepsilon_e$ it also is straightforward to show that eqn (2.3) with eqns (2.5) and (2.6) is consistent with

$$\sigma_{ij}\varepsilon_{ij} = \sigma_e \varepsilon_e \tag{2.7}$$

and, furthermore, that the stress is derivable from the strain energy function

$$W(\varepsilon) = \int_0^{\varepsilon} \sigma_{ij}\, d\varepsilon_{ij} = \int_0^{\varepsilon_e} \sigma_e\, d\varepsilon_e \tag{2.8}$$

as

$$s_{ij} = \frac{\partial W}{\partial \varepsilon_{ij}}. \tag{2.9}$$

For the study of neck propagation it is useful to plot the tensile behavior in terms of nominal or engineering stress (n) versus stretch (λ) for a material element as shown in Fig. 4. The nominal stress is force per unit initial area, $n = P/A_0$, and the stretch is the relative extension of a material line element. For incompressible materials under both uniaxial and plane strain tension, $n = \sigma/\lambda$. With eqn (2.1) taken as the relation between the effective true stress and the effective logarithmic strain and recalling that in plane strain tension $\sigma_e = (\sqrt{3}/2)\sigma$ and $\varepsilon_e = (2/\sqrt{3})\varepsilon$, the uniaxial plane strain behavior in the direction of stretching can be written in terms of n and λ. Figure 4 is the resulting plot with the material properties given in eqn (2.2).

Steady, plane strain neck propagation in an elastic material can be analyzed simply in terms of jump conditions following the analysis of Hutchinson and Neale[4]. For sufficiently slow deformation, dynamic effects can be neglected and the governing equations follow from conservation of mass and energy. As depicted in Fig. 5, consider at time t a control mass containing a fully developed neck (steady state) propagating with velocity c. The necked end is pulled with a velocity v by the constant force $P_N = P_U = P^* = n^* h_0$, where h_0 is the initial thickness and the corresponding axial stretches in the necked (N) and unnecked (U) regions are denoted λ_N and λ_U. The through thickness stretches are h_N/h_0 and h_U/h_0. At an instant Δt later the neck has propagated a distance $c\,\Delta t$, which is also shown in Fig. 5, and the shaded region denotes the same configuration as the shaded region shown at time t. Conservation of mass for this control mass leads to

$$(v+c)h_N = ch_U \tag{2.10}$$

or

$$v/c = h_U/h_N - 1. \tag{2.11}$$

Since for incompressible plane strain deformations $\lambda_U(h_U/h_0) = \lambda_N(h_N/h_0) = 1$, $h_U/h_N = \lambda_N/\lambda_U$ so that eqn (2.11) can also be written as

$$v/c = \lambda_N/\lambda_U - 1. \tag{2.12}$$

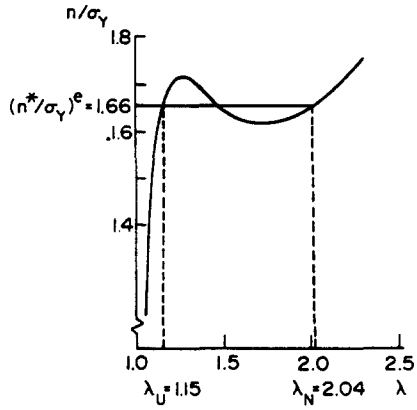

Fig. 4. Normalized uniaxial nominal stress (n/σ_Y) stretch (λ) curve for a polymer with σ–ε behavior described by eqn (2.2) and Fig. 2(b).

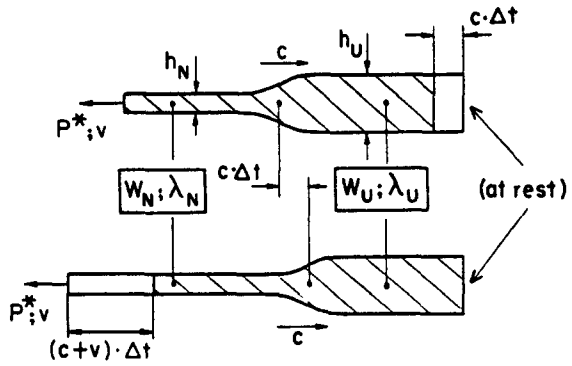

Fig. 5. Control mass, depicted at time $t = t_0$ and $t_0+\Delta t$, that illustrates conservation of mass and energy during steady-state neck propagation [eqns (2.10) and (2.13)]. Note that the shaded regions are identical in the two configurations.

With dynamic and thermal effects neglected, conservation of energy for the control mass requires that the rate of work input equals the rate of change of strain energy:

$$P^*v = W_N h_N(c+v) - W_U h_U c. \tag{2.13}$$

With $P^* = n^* h_0$ and $\lambda_U = h_0/h_U$, substitution of eqns (2.10) and (2.12) into eqn (2.13) yields

$$n^*(\lambda_N - \lambda_U) = W_N - W_U. \tag{2.14}$$

For plane strain tensile states the strain energy density is expressible simply in terms of the axial measures as

$$W = \int_0^\varepsilon \sigma \, d\varepsilon = \int_1^\lambda n \, d\lambda \tag{2.15}$$

and it follows that

$$W_N - W_U = \int_{\lambda_U}^{\lambda_N} n \, d\lambda. \tag{2.16}$$

That is, for an elastic material, the difference in strain energy between two deformed states is independent of the straining history taken between the two states. With eqn (2.16), eqn (2.14) can be written in a form that suggests a simple graphical solution:

$$n^*(\lambda_N - \lambda_U) = \int_{\lambda_U}^{\lambda_N} n \, d\lambda. \tag{2.17}$$

This solution is a statement that the area under the n vs λ curve (Fig. 4) between λ_U and λ_N equals the rectangular area $n^*(\lambda_N - \lambda_U)$. Equivalently, the area of the two lobes, one above and one below n^* in Fig. 4, must be equal. (In the case of phase transformations, the line at n^* connecting states U and N is called the Maxwell line; eqns (2.16) and (2.17) correspond to eqns (2.2) and (2.10) in [4].) For the material properties given in eqn (2.2) which were used to plot Fig. 4, $n^* = 1.66\sigma_Y$ and $\lambda_N/\lambda_U = 1.77$. This result can be compared with the axisymmetric result[4] that gives for the material properties of eqn (2.2), $n^* = 1.33\sigma_Y$ and $\lambda_N/\lambda_U = 2.34$.

3. ELASTIC-PLASTIC CONSTITUTIVE RELATIONS AND FINITE ELEMENT METHOD

In this section the finite strain elastic-plastic constitutive equations based on J_2-flow theory are reviewed[6, 7]. These equations are incorporated in an incremental, tangent

stiffness finite element algorithm[7–9]. The finite element equations are derived and certain aspects of the solution strategy are discussed.

3.1. *Finite strain, J_2-flow theory*

Let $\mathbf{x}$ denote the current position of a material point initially at $\mathbf{X}$. With the displacement vector $\mathbf{u} = \mathbf{x} - \mathbf{X}$, the deformation gradient $\mathbf{F}$ is defined by $d\mathbf{x} = \mathbf{F} \cdot d\mathbf{X}$. The rate of stretching tensor $\mathbf{d}$, which is the symmetric part of the velocity gradient, is expressed in terms of $\mathbf{F}$ as

$$\mathbf{d} = \tfrac{1}{2}[\dot{\mathbf{F}} \cdot \mathbf{F}^{-1} + (\mathbf{F}^{-1})^T \cdot \dot{\mathbf{F}}^T], \tag{3.1}$$

where the dot over a variable denotes a derivative with respect to a time-like loading parameter. The work-rate conjugate stress measure to $\mathbf{d}$ is the Kirchhoff stress $\boldsymbol{\tau}$ that is related to the Cauchy stress $\boldsymbol{\sigma}$ as

$$\boldsymbol{\tau} = (\rho_0/\rho)\boldsymbol{\sigma}, \tag{3.2}$$

where ρ_0/ρ is the ratio of the initial and current density of a material point.

The rate form of the constitutive relation is expressed in terms of the Jaumann derivative of the Kirchhoff stress

$$\overset{\nabla}{\boldsymbol{\tau}} = \dot{\boldsymbol{\tau}}^c + \mathbf{d} \cdot \boldsymbol{\tau} + \boldsymbol{\tau} \cdot \mathbf{d}, \tag{3.3}$$

which is an objective stress-rate measure. Here, $\dot{\boldsymbol{\tau}}^c$ denotes the convective derivative, i.e. the time-like $(\partial/\partial t)$ derivative of $\boldsymbol{\tau}$ in a material fixed coordinate system. With $\mathbf{C}$ denoting the fourth-order tensor of instantaneous moduli

$$\overset{\nabla}{\boldsymbol{\tau}} = \mathbf{C} : \mathbf{d}, \tag{3.4}$$

where the colon denotes a dyadic product. The components of $\mathbf{C}$ are given with respect to an arbitrary curvilinear coordinate system in the current configuration with covariant and contravariant base vectors $\boldsymbol{\varepsilon}_i$ and $\boldsymbol{\varepsilon}^i$, $i = 1, 3$, respectively. The covariant and contravariant components of the metric tensor in the current configuration $\mathbf{g} = g_{ij}\boldsymbol{\varepsilon}^i\boldsymbol{\varepsilon}^j = g^{ij}\boldsymbol{\varepsilon}_i\boldsymbol{\varepsilon}_j$, respectively, are $g_{ij} = \boldsymbol{\varepsilon}_i \cdot \boldsymbol{\varepsilon}_j$ and $g^{ij} = \boldsymbol{\varepsilon}^i \cdot \boldsymbol{\varepsilon}^j$.

Hutchinson[6] introduced a finite strain generalization of the isotropic hardening, J_2-flow theory of plasticity that expresses the contravariant components of $\mathbf{C}$ as

$$C^{ijkl} = \frac{E}{1+\nu}\left[\frac{1}{2}(g^{ik}g^{jl} + g^{jk}g^{il}) + \frac{\nu}{1-2\nu}g^{ij}g^{kl} - \frac{\alpha}{q}s^{ij}s^{kl}\right], \tag{3.5}$$

where $\mathbf{s}$ is the Kirchhoff stress-deviator tensor:

$$s^{ij} = g^{ik}g^{jl}s_{kl} = \tau^{ij} - \tfrac{1}{3}g^{ij}g_{kl}\tau^{kl}. \tag{3.6}$$

The second invariant (J_2) of $\mathbf{s}$ is the effective stress

$$\tau_e = (\tfrac{3}{2}s_{ij}s^{ij})^{1/2}. \tag{3.7}$$

The material parameters in eqn (3.5) are Young's modulus E, Poisson's ratio ν and the hardening parameter

$$q = (1+\nu)\frac{h}{E} + \frac{2}{3}\tau_e^2, \tag{3.8a}$$

where

$$\frac{1}{h}=\left(\frac{3}{2\tau_e}\right)^2\left\{\frac{\rho}{\rho_0}\left[1-(1-2\nu)\frac{\tau_e}{E}\right]\frac{1}{E_t}-\frac{1}{E}\right\}. \tag{3.8b}$$

Here E_t is the tangent modulus $d\sigma/d\varepsilon$ at the stress level $(\rho/\rho_0)\,\tau_e$ of the σ–ε curve in uniaxial tension. The switching parameter α in eqn (3.5) that distinguishes plastic loading ($\alpha = 1$) and elastic unloading ($\alpha = 0$) is defined in terms of

$$\alpha=\begin{cases}1 & \text{if } \tau_e=(\tau_e)_{\max} \text{ and } s^{ij}d_{ij}>0\\ 0 & \text{if } \tau_e<(\tau_e)_{\max}, \text{ or}\\ & \tau_e=(\tau_e)_{\max} \text{ and } s^{ij}d_{ij}\leqslant 0,\end{cases} \tag{3.9}$$

where $(\tau_e)_{\max}$ is the maximum value of τ_e that a material point has experienced up to the current state if yielding has occurred, otherwise $(\tau_e)_{\max}$ has the value at initial yield.

3.2. *Finite element formulation*

The finite element program developed for this analysis is based on a convected coordinate formulation[10], where the convected coordinates ξ^i are particle labels. This coordinate net is embedded in the initial configuration and deforms with the solid. This scheme is Lagrangian in character and has been discussed by Hutchinson[6] and Needleman[7].

The calculation is an incremental one where each solution increment approximately satisfies a rate form of the principle of virtual work. With body forces neglected, the equilibrium equation expressed in terms of the nominal or first Piola–Kirchhoff stress tensor, $\mathbf{n}(\xi^i, t) = \mathbf{F}^{-1}\cdot\boldsymbol{\tau}$,

$$n^{ij}_{,i}=0, \tag{3.10}$$

where $,i$ denotes $\partial/\partial\xi^i$. The principle of virtual work in terms of kinematically admissible virtual displacement δu_i is

$$\int_V n^{ij}\,\delta u_{j,i}\,dV=\int_S T^j\delta u_j\,dS, \tag{3.11}$$

where the nominal traction vector $\mathbf{T} = \boldsymbol{\nu}\cdot\mathbf{n}$, $\boldsymbol{\nu}$ being the unit outward normal to the surface in the reference configuration, and V and S are the volume and surface in the reference configuration. This equation governs the displacement-based finite element calculation used in the present work. Since it is nonlinear in displacements, a Newton iteration is used to obtain approximate solutions. The resulting equations resemble the rate form of the principle of virtual work, which is summarized below.

In terms of the nominal stress-rate and traction-rate, the rate form of the principle of virtual work is[7]:

$$\int_V \dot{n}^{ij}\delta u_{j,i}\,dV=\int_S \dot{T}^j\delta u_j\,dS. \tag{3.12}$$

Needleman[7] shows that with the constitutive equation (3.4) that eqn (3.12) can be expressed as

$$\int_V K^{ijkl}\dot{u}_{l,k}\delta u_{j,i}\,dV=\int_S \dot{T}^j\delta u_j\,dS, \tag{3.13}$$

where

$$K^{ijkl} = L^{piqk}F^{l}_{q}F^{j}_{p} + \tau^{ik}G^{jl}. \tag{3.14}$$

Here F^{i}_{j} are the mixed components of the deformation gradient and **G** is the reference configuration metric tensor. The components of the fourth order tensor **L** are expressed in terms of the incremental moduli **C** as[7]:

$$L^{ijkl} = C^{ijkl} - \tfrac{1}{2}[g^{ik}\tau^{jl} + g^{jk}\tau^{il} + g^{il}\tau^{jk} + g^{jl}\tau^{ik}]. \tag{3.15}$$

With the solution given at time t, eqn (3.11), with $\mathbf{T}(t+\Delta t)$ on the right-hand side, is solved for $\mathbf{u}(t+\Delta t)$. Let d( ) denote an increment in ( ) that is calculated via a Newton iteration, and let $dn^{ij} = K^{ijkl}\,du_{l,k}$, where **K** is based on the current estimate of **u**. Then, a Taylor series expansion of eqn (3.11) about the current estimate and the usual Newton approximation yields the governing equation for the finite element calculation

$$\int_V K^{ijkl}\,du_{l,k}\delta u_{j,i}\,dV = \int_S T^{j}\delta u_j\,dS - \int_V n^{ij}\delta u_{j,i}\,dV, \tag{3.16}$$

where, on the right-hand side, **T** is prescribed at $t+\Delta t$ and **n** is based on the current estimate for **u**. A nonzero contribution on the right-hand side of eqn (3.16) corrects for the lack of equilibrium in the estimate of the solution at $t+\Delta t$. Since $\mathbf{n}(t)$ is the initial estimate used on the right-hand side of eqn (3.16), the first iteration gives the solution of eqn (3.13) with $\Delta\mathbf{u} = d\mathbf{u} = \dot{\mathbf{u}}\Delta t$.

3.3. *Solution algorithm*

A standard displacement-based finite element discretization of eqn (3.16) yields a set of linear simultaneous equations for the iterative solution procedure. With $\{U\}$ denoting the vector of nodal displacements, the $n+1$ approximation to $\{U(t+\Delta t)\}$ is given as $\{U^{(n)}\}+\{dU^{(n)}\}$, where

$$[K^{(n)}]\{dU^{(n)}\} = \{dF^{(n)}\}. \tag{3.17}$$

Note that both the stiffness matrix $[K]$ and the right-hand-side vector $\{dF\}$ depends on the current estimate $\{U^{(n)}\}$. Once a convergence criterion is met, say after N iterations ($n = 1, N$), then the set of nodal displacements that approximately satisfies eqn (3.11) is

$$\begin{aligned} U(t+\Delta t) &= \{U(t)\} + \{\Delta U\} \\ &= \{U(t)\} + \sum_{n=1}^{N} \{dU^{(n)}\}. \end{aligned} \tag{3.18}$$

Recall that if $N = 1$, the d's in eqn (3.17) can be replaced by Δ's where the $\{\Delta F\}$ term is the vector of nodal force increments for the step Δt, and the solution $\{\Delta U\}$ is a finite element solution to eqn (3.12) with $\dot{(\ )} = \Delta(\ )/\Delta t$.

The convergence criterion chosen for the present work is

$$\left\{\sum_{j=1}^{\mathrm{NDF}} (dU_j^{(n)})^2 \Big/ \sum_{j=1}^{\mathrm{NDF}} \left(\sum_{i=1}^{n} dU_j^{(i)}\right)^2\right\}^{1/2} < 10^{-4}, \tag{3.19}$$

where NDF is the total number of nodal degrees of freedom. This tolerance should yield a solution with an average of three significant digits.

A special feature of the solution algorithm for updating stresses at the spatial integration points within elements is given below. Let a given element have P degrees of freedom

and let **B** be the strain–displacement matrix where

$$\dot{u}^j_i = \sum_{p=1}^{P} B^j_{ip} \dot{U}_p. \tag{3.20}$$

The calculated nodal displacement increments together with the constitutive relation are used to update the stresses[7]

$$\begin{aligned} \tau^{ij}(t+\Delta t) &= \tau^{ij}(t) + \int_t^{t+\Delta t} \dot{\tau}^{ij}\, \mathrm{d}t \\ &= \tau^{ij}(t) + \sum_{p=1}^{P} \int_{U(t)}^{U(t)+\Delta U} L^{ijkl} F^m_k B_{mlp}\, \mathrm{d}U_p. \end{aligned} \tag{3.21}$$

The integrals in eqn (3.21) are calculated from Euler's method with S subdivisions of $\Delta \mathbf{U}$ to yield

$$\tau^{ij}(t+\Delta t) = \tau^{ij}(t) + \sum_{s=1}^{S} \sum_{p=1}^{P} \left(L^{ijkl} F^m_k B_{mlp} \frac{\Delta U_p}{S} \right)\Bigg|_{U + \frac{s-1}{S}\Delta U}, \tag{3.22}$$

where the moduli, **L**, and the deformation gradient, **F**, vary with s. Alternative stress integration schemes include the radial return algorithm[11].

In general, for computational efficiency, the number of subdivisions, S, required for accurate spatial integration at a given point scales with the degree of nonlinearity of the integrand in eqn (3.21). In this work S is determined from a criterion based on the finite changes in deformation at each element integration point as described below. From the polar decomposition theorem it is known that any deformation state, **F**, can be obtained by a pure rotation, **R**, in series with a stretching operation, $\bar{\mathbf{U}}$:

$$\mathbf{F} = \mathbf{R} \cdot \bar{\mathbf{U}}. \tag{3.23}$$

For plane problems the rotation increment, $\Delta\Theta$, which is calculated from **R**, and the increment in the Mises effective-measure of the Green strain, $\Delta\eta_e$, which is calculated from $\bar{\mathbf{U}}$, provide a two-parameter description of the deformation increment. Automatic control of S during the calculation at each element integration-point is obtained through the algorithm[9]

$$S = \max(S_1, S_2), \tag{3.24}$$

where, for some N_1 and N_2,

$$\begin{aligned} S_1 &= N_1 \Delta\Theta, \\ S_2 &= N_2 \Delta\eta_e. \end{aligned} \tag{3.25}$$

The allowable step size using this algorithm was carefully investigated for two test problems: one-element plane strain tension with superimposed rotations and pure bending (25 elements).

To test the limits of the stress integration scheme the one-element calculations were carried out using no Newton equilibrium iterations. These results lead to $N_1 = 1500$ ($\Delta\Theta$ is in radians) and $N_2 = 1200$ for accurate results. Therefore, $S_1 = 26$ for a one degree rotation increment and $S_2 = 12$ for a strain increment of 0.01. After either a unit strain or 45° rotation of the one-element model, only a 2½% error in the maximum stress had accumulated. It was also observed that a fixed degree of accuracy could be achieved for a given product of the number of load steps times the number of stress intervals, S [9].

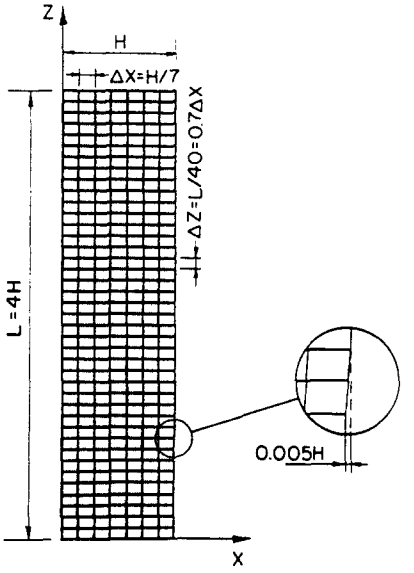

Fig. 6. Finite element mesh used to model one quadrant of the specimen ($7 \times 40 = 280$ elements).

4. NUMERICAL RESULTS AND DISCUSSION

Based upon a finite strain version of J_2-flow theory, eqn (3.5), with the uniaxial behavior of eqn (2.2), a finite element solution is presented for a neck that develops and propagates in an initially smooth specimen. Results presented include the overall load–deflection curve, the draw ratio, the stress and strain in the minimum section, and the triaxial stress distribution in the region of the neck. Some aspects of the numerical scheme and the effect of a nonlinear elastic constitutive law on the finite element calculation also are discussed at the end of the section.

The specimen modeled has a length to thickness ratio of 4. The mesh is depicted in Fig. 6 and consists of 280 elements forming one quadrant of the symmetric specimen. The elements are the superelement quadrilaterals first suggested by Nagtegaal *et al.*[12], which consists of four constant strain triangles. A "microscopic" imperfection in the mesh is used to initiate the neck formation. This is done by reducing the thickness of the center part of the specimen 0.5% along one-fourth of its length. The specimen is deformed by imposing axial displacement increments at the free end without restraining lateral movement. Thus the loading is displacement controlled and shear free.

The finite element results show uniform deformation up to load maximum which, for the material law chosen, is reached at an overall elongation of $\Delta/L_0 = 0.255$. The development of the neck is depicted in Fig. 7 as a series of consecutive deformation states (deformed mesh). The corresponding position of each state on the normalized load–elongation ($P/P_Y - \Delta/L_0$) curve is indicated in Fig. 8(a), where P_Y is the load at initial yield. This computed curve is in close qualitative agreement with experimental observation, e.g. Fig. 2(b). The stress and strain at the minimum sections corresponding to each state in Fig. 7 is shown in Fig. 8(b). The localization phenomenon also is illustrated in Fig. 9 through a plot of the draw ratio ($DR = \lambda_N/\lambda_U$) versus overall deformation (Δ/L_0), where λ_N and λ_U are calculated as initial thickness over current thickness at the center of the neck and at the end of the specimen, respectively ($\lambda_N = h_0/h_N$; $\lambda_U = h_0/h_U$).

Figures 8 and 9 show how both the load and draw ratio smoothly approach steady state propagation values, which differ from the values calculated in Section 2 for an elastic material. The effects of plasticity on the draw ratio and the propagation load, as contrasted with the results for an elastic material, are closely linked to the detailed shape of the uniaxial true stress–logarithmic strain curve. The difference between the elastic steady-state solution and the one based on a J_2-flow theory constitutive relation can be seen as the net result of

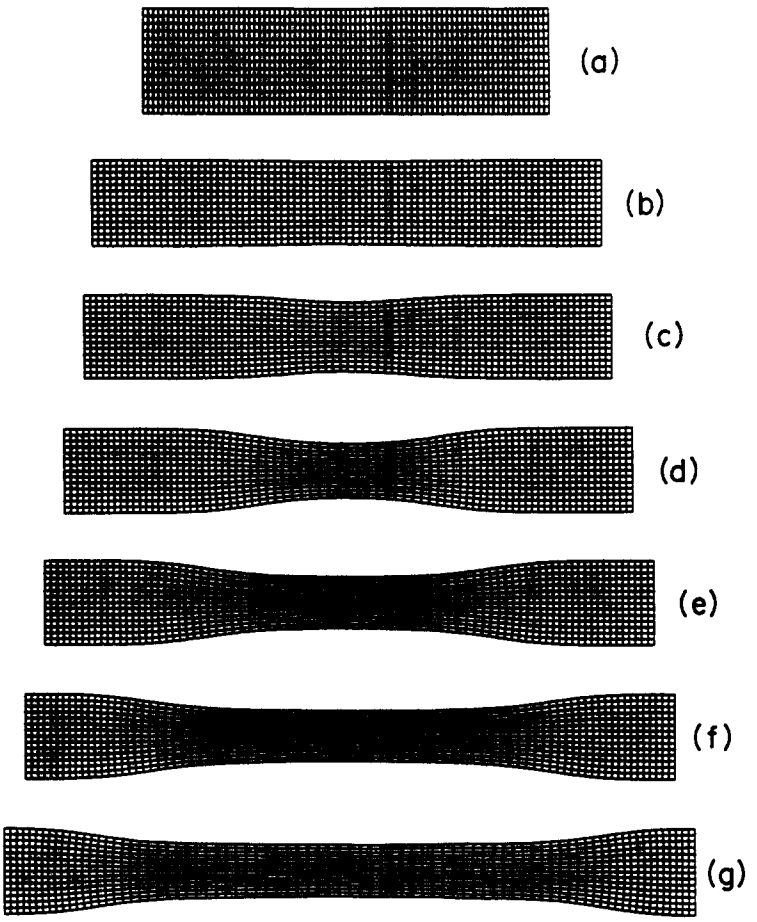

Fig. 7. Finite element results for neck formation and propagation depicted as a series of deformation states (deformed mesh).

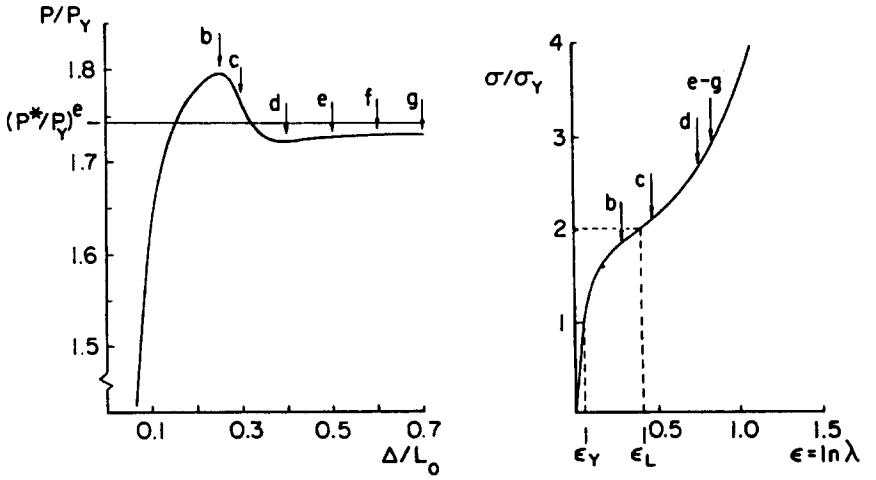

Fig. 8. (a) Finite element results for normalized load (P/P_Y)–elongation (Δ/L_0) during neck formation and propagation. The labeled arrows correspond to the deformation states in Fig. 7 and (b) position on the σ–ε curve of material points at the center of the minimum section of the deformation states in Fig. 7.

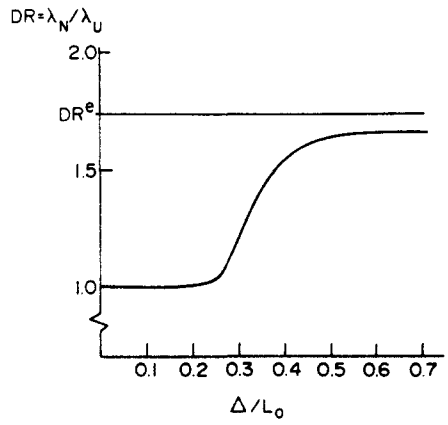

Fig. 9. Finite element results for draw ratio ($DR = \lambda_N/\lambda_U$) as a function of elongation (Δ/L_0).

two competing effects. The stiffer unloading in the unnecked region during neck formation exhibited by the flow theory material yields a higher stretch in the unnecked region ($\lambda_U^{e-p} = 1.23$; $\lambda_U^e = 1.15$). This would suggest a lower draw ratio and consequently also a lower propagation load. On the other hand, the dissipative nature of plastic work together with a relatively stiff response of flow theories to nonproportional stressing indicates a higher propagation load. In this study both the propagation load and the draw ratio are lower for the elastic-plastic material, $(P^*/P_Y)^{e-p} = 1.73$; $DR^{e-p} = 1.66$, compared to $(P^*/P_Y)^e = 1.75$; $DR^e = 1.77$ for corresponding elastic material. For materials with uniaxial behavior leading to higher draw ratios the energy dissipation is likely to dominate (more shear deformation) resulting in both higher propagation load and draw ratio for the elastic-plastic case than for corresponding elastic case. Neale and Tugcu[5] recently presented a finite element analysis of neck propagation in axisymmetric bars where this latter situation occurs. For the σ–ε curve chosen in [5] the elastic draw ratio, $DR^e = 3.61$, and propagation load, $(P^*/P_Y)^e = 1.11$ is predicted in simple tension, while the finite element calculation give $DR^{e-p} = 3.82$ and $(P^*/P_Y)^{e-p} = 1.23$ for a J_2-flow theory material. As a comparison this uniaxial curve would yield $DR^e = 2.45$ and $(P^*/P_Y)^e = 1.43$ for an elastic material in plane strain tension.

For the present case the calculations were terminated at overall elongation $\Delta/L_0 = 0.7$ when the transition region reached the end of the specimen. At this stage nearly steady-state conditions are attained, and the increase in DR and P/P_Y during the late part of the calculation is small. It should be noted that truly steady-state conditions cannot be obtained until the transition region has completely propagated away from the site of neck formation, since the stress history during the development of the neck differs from the steady-state history. In Fig. 10 the degree of steady state is illustrated by plotting the stresses along the center line of the specimen for two consecutive stages of the propagation phase, $\Delta/L_0 = 0.5$ and $\Delta/L_0 = 0.7$. Figure 10 also shows that the convex part of the neck profile corresponds to compressive transverse stress, σ_{xx}, while the concave portion has tensile σ_{xx} (G'Sell *et al.*[3]).

In Fig. 11 the stress distribution across the minimum section is shown during the development of the neck. At load maximum ($\Delta/L_0 = 0.255$) the uniform stress field is only perturbed by the initial imperfection. When the neck starts to develop the stresses are nonuniform (similar to [5]) with the highest stresses at the center of the plate and the magnitudes decreasing toward the surface. For this calculation a uniform stress field in the minimum section is approached at steady state. Neale and Tugcu's axisymmetric calculation showed nonuniform stresses across the minimum section at steady state with maximum values at the surface. It is not clear whether the difference is caused primarily by the difference in deformation state (plane strain or simple tension) or mainly by the different magnitude of draw ratios.

The buildup of hydrostatic tension at the minimum section during neck formation can

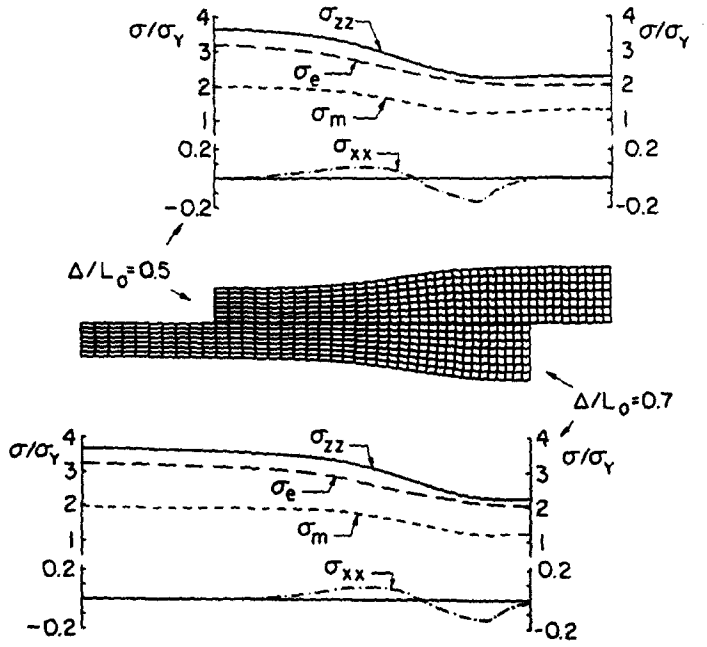

Fig. 10. Stresses along the specimen center line at two deformation states, $\Delta/L_0 = 0.5$ (top) and 0.7 (bottom), that illustrates nearly steady-state conditions. Deformed meshes are positioned with nearly identical regions juxtaposed.

be shown by plotting a plane strain counterpart to the Bridgeman[3, 13] triaxiality factor in uniaxial tension, F_T, versus elongation, Δ/L_0 (Fig. 12). Here F_T is taken as

$$F_T = \frac{1}{\sqrt{3}} \cdot \frac{\bar{\tau}_e}{\bar{\sigma}_m}, \tag{4.1}$$

where $\bar{\tau}_e/\bar{\sigma}_m$ is the ratio of average effective Kirchhoff stress to the average hydrostatic tension at minimum cross-section and $1/\sqrt{3}$ is a normalizing constant to give $F_T = 1$ in uniform plane strain tension. A comparison of Figs 7, 8 and 12, shows that as the neck

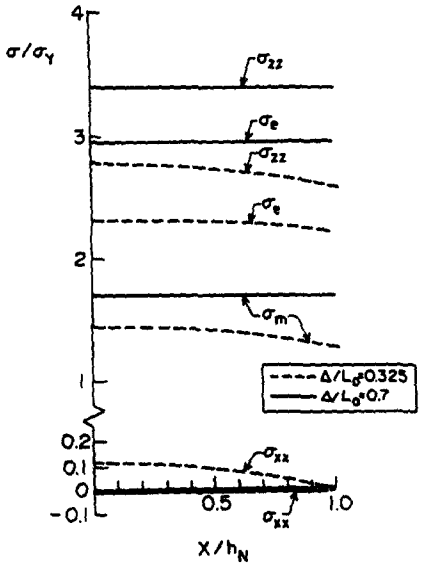

Fig. 11. Stress distribution across the minimum section during neck formation ($\Delta/L_0 = 0.325$) and during propagation ($\Delta/L_0 = 0.7$).

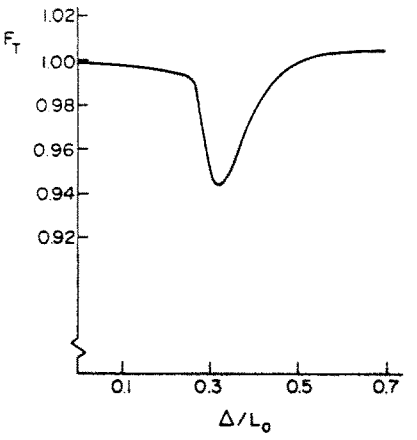

Fig. 12. The triaxiality factor, $F_T = (1/\sqrt{3}) \cdot (\bar{\sigma}_e/\bar{\sigma}_m)$ at the minimum cross-section versus elongation, Δ/L_0.

develops the triaxiality increases, which corresponds to $F_T < 1$. As a consequence, the uniaxial stresses and strains in the region $0.25 < \varepsilon < 0.5$ of the uniaxial plot in Fig. 8(b) are not measurable in a straightforward manner.

The finite element calculation summarized in Fig. 7 resulted from 940 displacement increments using about 80 CPU hours and a VAX 11/780 computer. The stepsize was manually adjusted during the computation so that no more than four equilibrium iterations were required for a given increment. An updated stiffness matrix is used in the iteration scheme, and the convergence criterion yields displacement increments with an average of three significant digits. The switch parameter, α, in the constitutive law, eqn (3.5), is updated only between increments. By holding α constant during each step the path independence of the solution increments is kept and the use of equilibrium iterations is justified. The overall strain increments used in the beginning of the calculation was $\Delta e = (\Delta(t+\mathrm{d}t) - \Delta(t))/L_0 = 0.005$. Close to load maximum this value had to be reduced to a value, $\Delta e = 0.0005$, which was kept through the remainder of the calculation.

An interesting phenomenon occurred when a finite element calculation was attempted that used a finite strain version of J_2-deformation theory without linear elastic unloading. The calculation had to be terminated shortly after load maximum since the equilibrium iterations failed to converge. It was observed that the $(P/P_Y) - (\Delta/L_0)$ curve had turned vertically downward (i.e. $\mathrm{d}P/\mathrm{d}\Delta \to -\infty$) and consequently, the end displacement could not be increased. This structural instability is a result of the decrease in load after load maximum which causes the strain in the region outside the neck to decrease while the neck is forming. This in turn causes an overall decrease in length which is proportional to the length of the unnecked region. The deformation theory unloads with stiffness of the current tangent modulus which, in this case, is about an order of magnitude lower than the initial elastic modulus used in the flow theory. Therefore, more displacement is recovered during the unloading using the deformation theory, which leads to the instability, when at same point the increase in length of the necking region is balanced by this recovery. The phenomenon has previously been observed by Tvergaard *et al.*[14] in their investigation of the flow localization in plane strain tensile tests. It should be noted that all materials that recover strain during unloading would show this behavior for long enough specimens.

Acknowledgements—The assistance to Dr. P. Burgers in program development during the initial stages of this work and the support of the National Science Foundation under Grant MEA 83-52172 are gratefully acknowledged.

REFERENCES

1. C. G'Sell and J. J. Jonas, Determination of the plastic behavior of solid polymers at constant true strain rate. *J. Mater. Sci.* **14**, 583 (1979).
2. R. J. Young, *Introduction to Polymers*. Chapman & Hall, London (1981).

3. C. G'Sell, N. A. Aly-Helal and J. J. Jonas, Effects of triaxiality on neck propagation during the tensile stretching of solid polymers. *J. Mater. Sci.* **18,** 1731 (1983).
4. J. W. Hutchinson and K. W. Neale, Neck propagation. *J. Mech. Phys. Solids* **31,** 405 (1983).
5. K. W. Neale and P. Tugcu, Analysis of necking and neck propagation in polymeric materials. *J. Mech. Phys. Solids* **33,** 323 (1985).
6. J. W. Hutchinson, Finite strain analysis of elastic–plastic solids and structures. In *Numerical Solutions of Nonlinear Structural Problems* (Edited by R. F. Hartung), p. 17. ASME (1973).
7. A. Needleman, Finite elements for finite strain plasticity problems. In *Plasticity of Metals at Finite Strain: Theory, Computation and Experiment* (Edited by E. H. Lee and R. L. Mallett), p. 387 (1982).
8. A. Needleman and V. Tvergaard, Finite element analysis. In *Finite Elements, Special Problems in Solid Mechanics* (Edited by J. T. Oden and G. F. Carey), Vol. V, p. 94 (1984).
9. L.-O. Fager, Finite element analysis of neck propagation in polymers. Master's thesis, University of Pennsylvania (1984).
10. A. E. Green and W. Zerna, *Theoretical Elasticity*. Oxford University Press, London (1954).
11. J. C. Nagtegaal, On the implementation of inelastic constitutive equations with special reference to large deformation problems. *Comp. Meth. Appl. Mech. Engng* **33,** 469 (1982).
12. J. C. Nagtegaal, D. M. Parks and J. R. Rice, On numerically accurate finite element solutions in the fully plastic range. *Comp. Meth. Appl. Mech. Engng* **4,** 63 (1978).
13. P. W. Bridgeman, *Studies in Large Plastic Flow and Fracture*. McGraw-Hill, New York (1952).
14. V. Tvergaard, A. Needleman and K. K. Lo, Flow localization in the plane strain tensile test. *J. Mech. Phys. Solids* **29,** 115 (1981).